Journal of Sound and Vibration 635 (2026) 119800

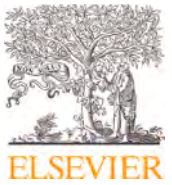

Contents lists available at ScienceDirect

Journal of Sound and Vibration

journal homepage: www.elsevier.com/locate/jsvi

Real-time implementation of delayed model predictive control in active noise control systems

Chao Liang [a,*], Francesco Ripamonti [a], Hamid Reza Karimi [a], Marek Pawełczyk [b]

[a] Department of Mechanical Engineering, Politecnico di Milano, Via Privata Giuseppe La Masa, 1, Milano, 20156, Italy
[b] Silesian University of Technology, Department of Measurements and Control Systems, Akademicka 16, Gliwice, 44–100, Poland

ARTICLE INFO

Keywords:
Active noise control
State-space model
Model predictive control
Time delay
Computational complexity

ABSTRACT

The filtered-x normalized least mean square (FxNLMS) algorithm is widely used in industrial active noise control (ANC) systems due to its simple implementation and robust stability. In contrast, model predictive control (MPC) is known for handling multivariable and constrained optimization problems but remains underutilized in active noise control due to its high computational demand and the strict latency requirements of ANC systems. Additionally, existing MPC based ANC schemes often rely on external disturbance predictors, limiting their accuracy and applicability to predictable noise. This paper addresses these shortcomings by formulating a delayed joint state space model that integrates the primary and secondary acoustic paths, thereby removing the need for disturbance prediction. Building on this model, we derive an unconstrained causal MPC algorithm combined with saturation that directly computes the optimal control signals for the secondary loudspeaker in real time. Compared to the standard FxNLMS algorithm, the proposed method achieves improved noise attenuation while maintaining computational complexity comparable to FxNLMS. The performance of the approach is demonstrated through numerical simulations and real time experiments.

1. Introduction

Active noise control (ANC), based on the principle of wave superposition, is widely adopted for attenuating primary noise. Among existing algorithms, the filtered-x normalized least mean square (FxNLMS) has become a standard due to its low computational complexity, simplicity and robust performance [1–3].

In contrast, model predictive control (MPC), renowned for handling multi-variable constrained optimization problems, has been extensively applied in active vibration control [4]. However, its application to ANC systems remains limited due to two main challenges: (i) the requirement for future disturbance information, violating the causal principle [5–7], and (ii) excessive computational complexity incompatible with the high sampling rates required in ANC [8,9].

To estimate future disturbances, various approaches have been proposed. [10] employs a state Kalman predictor, while [11] uses an autoregressive model. More recent studies have adopted ARX (Auto-Regressive with Exogenous inputs) structures [12,13], which have proven effective in handling periodic or deterministic disturbances. However, these predictive models exhibit limited applicability under broadband noise.

* Corresponding author.
E-mail addresses: chao.liang@polimi.it (C. Liang), francesco.ripamonti@polimi.it (F. Ripamonti), hamidreza.karimi@polimi.it (H.R. Karimi), marek.pawelczyk@polsl.pl (M. Pawełczyk).

https://doi.org/10.1016/j.jsv.2026.119800
Received 29 August 2025; Received in revised form 12 March 2026; Accepted 3 April 2026
Available online 5 April 2026

Table 1
Notation and symbol definitions.

Symbol	Dimension	Description
$(\cdot)_k$	scalar	Time instant of discrete system
$(\cdot)^p/(\cdot)^s$	-	Primary/Secondary path
u_k^p/u_k^s	scalar	Primary input/Secondary (control) input
y_k^p/y_k^s	scalar	Primary disturbance/Anti-noise
y_k	scalar	System output (error signal)
m/n	scalar	Order dimension of state-space model of primary/secondary path
$\mathbf{x}_k^p/\mathbf{x}_k^s$	$\mathbb{R}^m/\mathbb{R}^n$	State vector of the primary/secondary path
$\mathbf{x}_k$	$\mathbb{R}^{m+n}$	Augmented joint state vector
$\mathbf{A}^p/\mathbf{A}^s$	$\mathbb{R}^{m\times m}/\mathbb{R}^{n\times n}$	State matrix of the primary/secondary path
$\mathbf{B}^p/\mathbf{B}^s$	$\mathbb{R}^{m\times 1}/\mathbb{R}^{n\times 1}$	Input matrix of the primary/secondary path
$\mathbf{C}^p/\mathbf{C}^s$	$\mathbb{R}^{1\times m}/\mathbb{R}^{1\times n}$	Output matrix of the primary/secondary path
$\mathbf{D}^p/\mathbf{D}^s$	$\mathbb{R}^{1\times 1}$	Feedthrough matrix of the primary/secondary path
$\mathbf{A}$	$\mathbb{R}^{(m+n)\times(m+n)}$	Joint state matrix
$\mathbf{C}$	$\mathbb{R}^{1\times(m+n)}$	Joint output matrix
f	scalar	Prediction and control horizon
$\mathbf{u}^p/\mathbf{u}^s$	$\mathbb{R}^{f+1}$	Primary/Secondary input sequence over horizon
$\mathbf{y}$	$\mathbb{R}^f$	Predicted output (error) sequence
$\mathbf{O}$	$\mathbb{R}^{f\times(m+n)}$	State prediction matrix
$\mathbf{M}^p/\mathbf{M}^s$	$\mathbb{R}^{f\times(f+1)}$	Primary/Secondary input prediction matrix
$\mathbf{c}$	$\mathbb{R}^f$	Constant term in MPC prediction
$\mathbf{Q}$	$\mathbb{R}^{f\times f}$	Output weighting matrix
$\mathbf{R}/\mathbf{H}$	$\mathbb{R}^{(f+1)\times(f+1)}$	Control weighting matrix/Hessian matrix of MPC cost
$\mathbf{g}$	$\mathbb{R}^{f+1}$	Gradient vector of MPC cost
N_d^p/N_d^s	scalar	Primary/Secondary path delay (samples)
N_d	scalar	Delay difference $N_d^p - N_d^s$
$u_{\max}^s/u_{\min}^s$	scalar	Upper/Lower saturation bound of control input
$A_{\max}$	scalar	Maximum amplitude of primary input
d_k	scalar	Measured primary disturbance
a_k	scalar	Measured anti-noise
e_k	scalar	Measured error signal

Regarding computational complexity, conventional MPC involves solving a constrained optimization problem at each sampling instant, often exceeding real-time computational capabilities in ANC systems. To address this, explicit MPC [14] precomputes control laws in an offline "lookup table" for rapid retrieval. Yet, as the number of control variables increases, memory demand and table size grow exponentially. Alternatively, algorithms based on active-set and interior-point methods [15,16] improve convergence rates but still incur heavy computational loads compared to unconstrained methods.

Crucially, the inherent propagation delay in the ANC primary path offers a causal mechanism for predicting future disturbances using past measurements, eliminating the need for additional prediction models. While [17] exploited this delay-based mechanism using finite impulse response models, the associated computational cost made real-time implementation impractical.

To overcome these limitations, this study proposes a novel causal MPC-ANC framework incorporating three key points: (1) a low-order state-space model to reduce system dimensionality, (2) primary-path delay integration for causal disturbance estimation applicable to arbitrary noise types, and (3) unconstrained MPC scheme incorporating saturation handling to ensure feasibility while minimizing computational effort.

The main contributions are summarized as follows:

- An analytical closed-form solution of the ANC-oriented MPC is derived, which avoids iterative optimization and yields computational complexity on the same order as the conventional FxNLMS algorithm. This makes MPC practically feasible for real-time ANC implementation.
- A delay-embedded causal control strategy is proposed, where the introduction of a primary-path delay model eliminates the need for disturbance prediction. As a result, the framework is no longer restricted to predictable reference signals and can address arbitrary broadband noises.
- The proposed approach achieves real-time broadband noise attenuation with negligible convergence time. Even under rapidly varying reference signals, the controller is able to maintain effective attenuation.

These contributions are validated through comprehensive numerical simulations and experimental tests.

In this work, both the primary and secondary acoustic paths are assumed to be available through an offline identification stage. This assumption targets ANC applications in fixed or slowly varying acoustic environments, such as ducts, enclosures and laboratory test rigs. Specifically, the focus of this paper is on real-time predictive control under a finite preview horizon, rather than on acoustic path identification.

The paper is structured as follows: Section 2 details the MPC formulation, Sections 3–4 present numerical and experimental validations respectively, and Section 5 concludes the study and outlines future work.

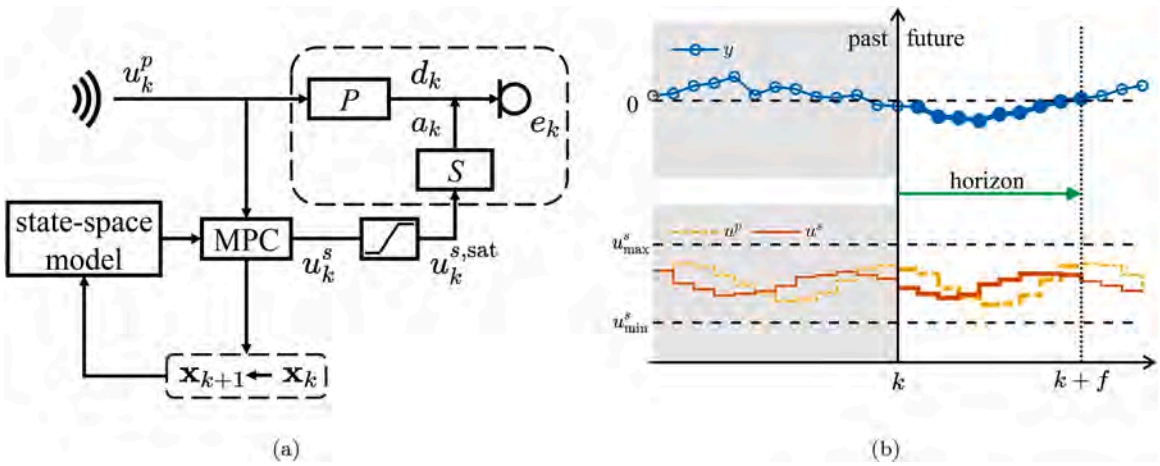

Fig. 1. MPC-based ANC without primary path delay. (a) System diagram. (b) Sampling instants. (For interpretation of the references to colour in this figure legend, the reader is referred to the web version of this article.)

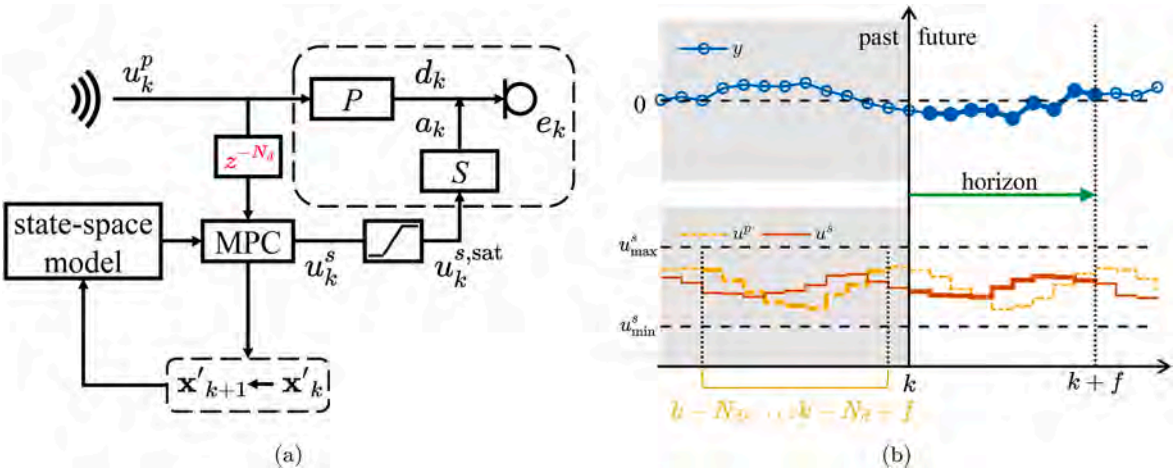

Fig. 2. MPC-based ANC with primary path delay. (a) System diagram. (b) Sampling instants. (For interpretation of the references to colour in this figure legend, the reader is referred to the web version of this article.)

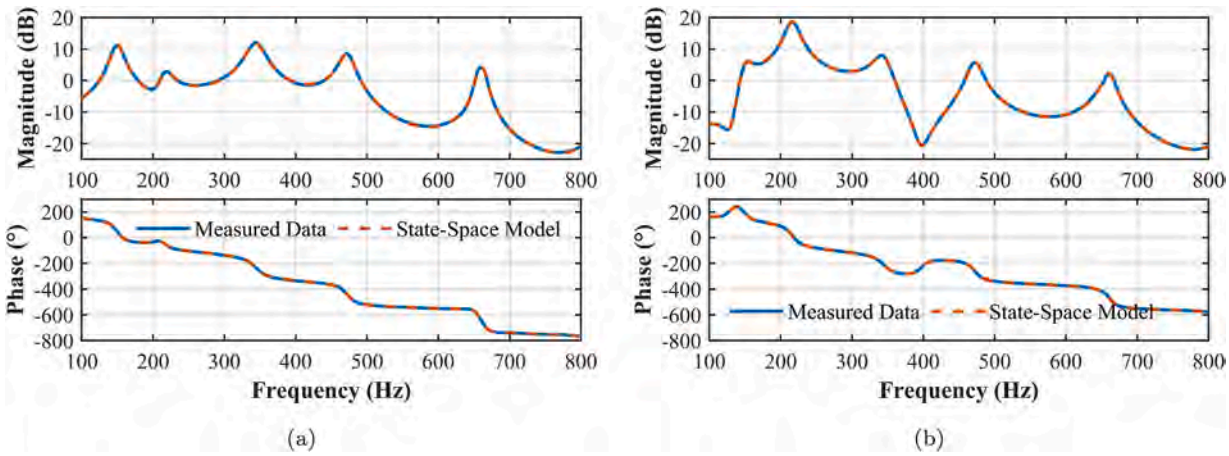

Fig. 3. Frequency response comparison between measured data and state-space model. (a) Primary path. (b) Secondary path.

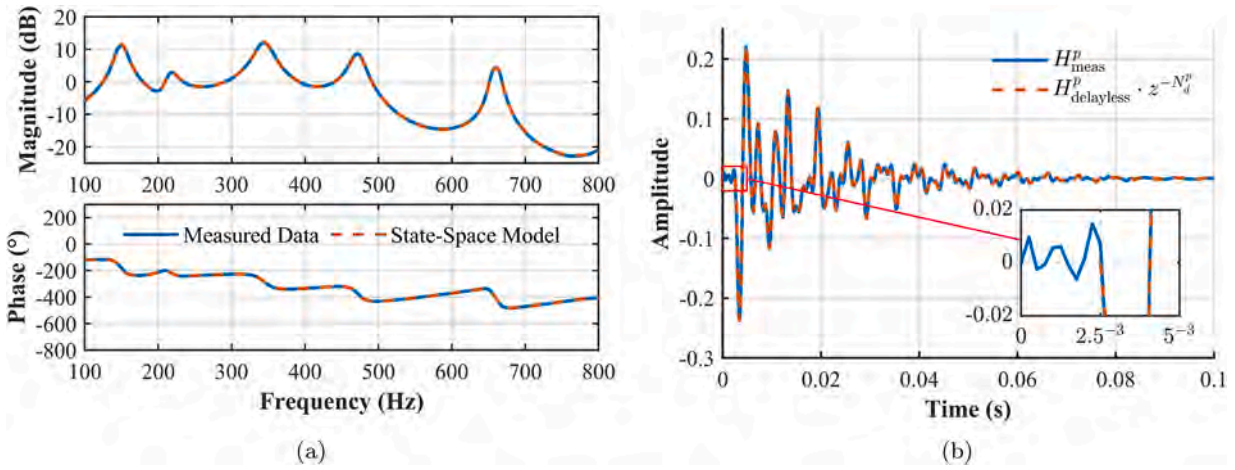

Fig. 4. Primary path characteristics. (a) Delayless primary path frequency response $H^p_{\text{delayless}}$. (b) Unit impulse response.

2. MPC formulation

2.1. Joint state-space model

The primary and secondary acoustic paths are denoted by superscripts p and s, respectively. The corresponding models are assumed to be available through prior identification and are modeled as the following discrete-time state-space systems:

$$\begin{cases} \mathbf{x}^p_{k+1} = \mathbf{A}^p \mathbf{x}^p_k + \mathbf{B}^p u^p_k, \\ y^p_k = \mathbf{C}^p \mathbf{x}^p_k + \mathbf{D}^p u^p_k, \end{cases} \tag{1}$$

and

$$\begin{cases} \mathbf{x}^s_{k+1} = \mathbf{A}^s \mathbf{x}^s_k + \mathbf{B}^s u^s_k, \\ y^s_k = \mathbf{C}^s \mathbf{x}^s_k + \mathbf{D}^s u^s_k, \end{cases} \tag{2}$$

where the subscript k denotes the discrete sampling instant. $\mathbf{A}^p \in \mathbb{R}^{m\times m}$, $\mathbf{B}^p \in \mathbb{R}^{m\times 1}$, $\mathbf{C}^p \in \mathbb{R}^{1\times m}$, $\mathbf{D}^p \in \mathbb{R}^{1\times 1}$. $\mathbf{A}^s \in \mathbb{R}^{n\times n}$, $\mathbf{B}^s \in \mathbb{R}^{n\times 1}$, $\mathbf{C}^s \in \mathbb{R}^{1\times n}$, $\mathbf{D}^s \in \mathbb{R}^{1\times 1}$. The variables u^p_k and u^s_k are the control inputs to the primary and secondary paths, respectively. The vectors $\mathbf{x}^p_k \in \mathbb{R}^m$ and $\mathbf{x}^s_k \in \mathbb{R}^n$ represent the corresponding state vectors, while y^p_k and y^s_k denote the primary disturbance and the generated anti-noise signal, respectively. For clarity, the notation used throughout the paper is summarized in Table 1. By combining the state-space models of both paths, the overall joint state-space representation of the active noise control system can be expressed as:

$$\begin{cases} \mathbf{x}_{k+1} = \underbrace{\begin{bmatrix} \mathbf{A}^p & 0 \\ 0 & \mathbf{A}^s \end{bmatrix}}_{\mathbf{A}} \mathbf{x}_k + \begin{bmatrix} \mathbf{B}^p \\ \mathbf{0} \end{bmatrix} u^p_k + \begin{bmatrix} 0 \\ \mathbf{B}^s \end{bmatrix} u^s_k, \\ y_k = y^p_k - y^s_k = \underbrace{\begin{bmatrix} \mathbf{C}^p & -\mathbf{C}^s \end{bmatrix}}_{\mathbf{C}} \mathbf{x}_k + \mathbf{D}^p u^p_k - \mathbf{D}^s u^s_k, \end{cases} \tag{3}$$

where y_k is the residual error signal to be minimized. $\mathbf{A} \in \mathbb{R}^{(m+n)\times(m+n)}$, $\mathbf{C} \in \mathbb{R}^{1\times(m+n)}$. The augmented state vector is defined as:

$$\mathbf{x}_k = \begin{bmatrix} \mathbf{x}^p_k \\ \mathbf{x}^s_k \end{bmatrix}. \tag{4}$$

Remark 1: In many practical feedforward ANC systems, only the secondary path is explicitly identified, while the primary path is typically unknown. In practice, an equivalent primary-path model (from the reference microphone signal to the error microphone signal) can be identified by standard system identification techniques using the reference and error microphone measurements when the control is inactive. The identified model can then be converted into an equivalent state-space representation and incorporated into the proposed MPC formulation. In this paper, we focus on the control design and real-time feasibility of the MPC scheme and assume that the acoustic path models are obtained in advance through an offline identification stage.

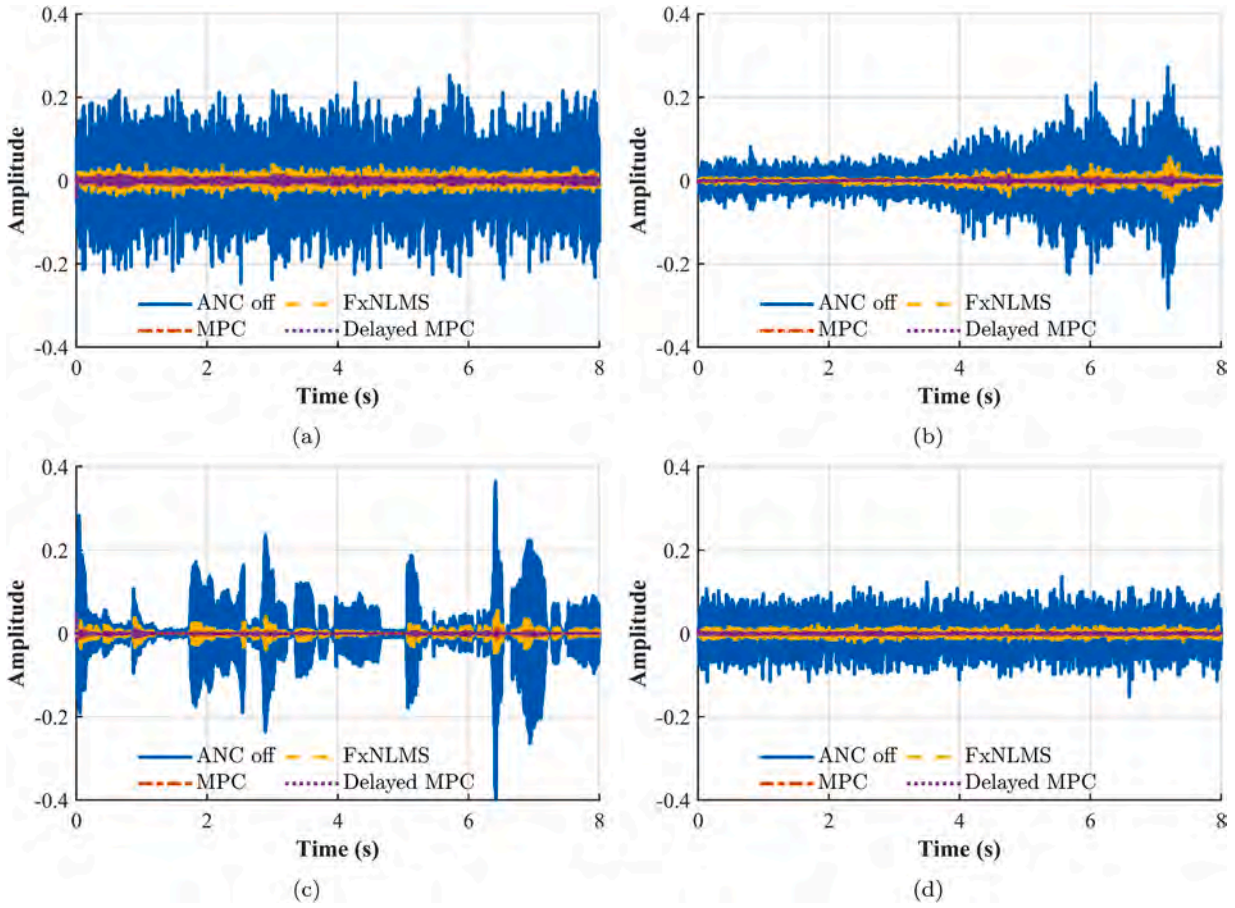

Fig. 5. Error signals for different noise types: (a) Traffic. (b) Airplane. (c) Human. (d) White. (For interpretation of the references to colour in this figure legend, the reader is referred to the web version of this article.)

2.2. Prediction over horizon f

Let f denote the prediction and control horizon. The future input sequences and the corresponding predicted output sequences over this horizon are defined as:

$$\mathbf{u}^p = \begin{bmatrix} u_k^p \\ \vdots \\ u_{k+f}^p \end{bmatrix}, \quad \mathbf{u}^s = \begin{bmatrix} u_k^s \\ \vdots \\ u_{k+f}^s \end{bmatrix}, \quad \mathbf{y} = \begin{bmatrix} y_{k+1} \\ \vdots \\ y_{k+f} \end{bmatrix}, \tag{5}$$

where $\mathbf{u}^p, \mathbf{u}^s \in \mathbb{R}^{f+1}$ and $\mathbf{y} \in \mathbb{R}^f$. To facilitate prediction over the horizon, define the following matrices:

$$\mathbf{O} = \begin{bmatrix} \mathbf{C}\mathbf{A} \\ \mathbf{C}\mathbf{A}^2 \\ \vdots \\ \mathbf{C}\mathbf{A}^f \end{bmatrix}, \quad \mathbf{M}^p = \begin{bmatrix} \mathbf{C}^p\mathbf{B}^p & \mathbf{D}^p & \cdots & 0 & 0 \\ \mathbf{C}^p\mathbf{A}^p\mathbf{B}^p & \mathbf{C}^p\mathbf{B}^p & \ddots & 0 & 0 \\ \vdots & \vdots & \ddots & \ddots & \vdots \\ \mathbf{C}^p\mathbf{A}^{p^{f-1}}\mathbf{B}^p & \mathbf{C}^p\mathbf{A}^{p^{f-2}}\mathbf{B}^p & \cdots & \mathbf{C}^p\mathbf{B}^p & \mathbf{D}^p \end{bmatrix}, \tag{6}$$

and

$$\mathbf{M}^s = \begin{bmatrix} \mathbf{C}^s\mathbf{B}^s & \mathbf{D}^s & \cdots & 0 & 0 \\ \mathbf{C}^s\mathbf{A}^s\mathbf{B}^s & \mathbf{C}^s\mathbf{B}^s & \ddots & 0 & 0 \\ \vdots & \vdots & \ddots & \ddots & \vdots \\ \mathbf{C}^s\mathbf{A}^{s^{f-1}}\mathbf{B}^s & \mathbf{C}^s\mathbf{A}^{s^{f-2}}\mathbf{B}^s & \cdots & \mathbf{C}^s\mathbf{B}^s & \mathbf{D}^s \end{bmatrix}, \tag{7}$$

where $\mathbf{O} \in \mathbb{R}^{f\times(m+n)}$ and $\mathbf{M}^p, \mathbf{M}^s \in \mathbb{R}^{f\times(f+1)}$. Next, define a known term with respect to the optimization variable $\mathbf{u}^s$:

$$\mathbf{c} = \mathbf{O}\,\mathbf{x}_k + \mathbf{M}^p\,\mathbf{u}^p, \tag{8}$$

which incorporates the contributions of the current system state and the future primary path inputs over the horizon. Accordingly, the predicted error sequence $\mathbf{y}$ over the horizon can be expressed as a function of the secondary control inputs $\mathbf{u}^s$ as follows:

$$\mathbf{y} = \mathbf{c} - \mathbf{M}^s \mathbf{u}^s. \tag{9}$$

2.3. MPC Cost and analytical solution

The cost function is defined as:

$$J(\mathbf{u}^s) = \mathbf{y}^T \mathbf{Q}\, \mathbf{y} + (\mathbf{u}^s)^T \mathbf{R}\, \mathbf{u}^s, \tag{10}$$

where $\mathbf{Q}$ and $\mathbf{R}$ are weighting matrices that penalize the predicted error and control effort , respectively. By setting $\partial J(\mathbf{u}^s)/\partial \mathbf{u}^s = 0$, the optimal control input sequence $\mathbf{u}^{s*}$ is obtained as:

$$\mathbf{u}^{s*} = \mathbf{H}^{-1}\mathbf{g}, \tag{11}$$

where

$$\mathbf{H} = \mathbf{M}^{sT}\mathbf{Q}\mathbf{M}^s + \mathbf{R}, \qquad \mathbf{g} = \mathbf{M}^{sT}\mathbf{Q}\,\mathbf{c}. \tag{12}$$

$\mathbf{u}^{s*}$ is taken as the optimal control sequence for the secondary path. It should be emphasized that the proposed method computes a signal-dependent optimal control sequence at each sampling instant, rather than a fixed controller mapping from the reference signal to the control signal. Note that Eq. (11) assumes that the future sequence $\mathbf{u}^p$ in Eq. (5) is known or can be predicted in advance.

At each control instant, only the first element of the optimal sequence, $u_k^s = \mathbf{u}^{s*}(1)$, is applied to the system. To ensure the control input remains within allowable bounds, a saturation function is imposed as follows:

$$u_k^{s,\mathrm{sat}} = \begin{cases} u^s_{\max}, & \text{if } u_k^s > u^s_{\max}, \\ u^s_{\min}, & \text{if } u_k^s < u^s_{\min}, \\ u_k^s, & \text{otherwise.} \end{cases} \tag{13}$$

Although the saturation does not explicitly solve a constrained MPC optimization problem, it provides a practical approximation when the unconstrained optimal solution remains within the admissible input bounds for most time instants. In such cases, the saturation is inactive and the resulting control action coincides with the solution of a constrained MPC formulation. The impact of active saturation on noise attenuation performance is explicitly investigated in Section 3.3.

2.4. Delayed system

In practical systems, delays between inputs and outputs are common. The measured transfer functions, denoted as H_{meas}, can be represented by their delay-free counterparts $H_{\mathrm{delayless}}$ along with corresponding delays as follows:

$$H^p_{\mathrm{meas}}(z) = H^p_{\mathrm{delayless}}(z)\cdot z^{-N_d^p}, \qquad H^s_{\mathrm{meas}}(z) = H^s_{\mathrm{delayless}}(z)\cdot z^{-N_d^s}, \tag{14}$$

where N_d^p and N_d^s represent the number of discrete-time sampling delays in the primary and secondary paths, respectively.

Accordingly, the state-space representation of the primary path becomes:

$$\begin{cases} \mathbf{x}^p_{k+1-N_d^p} = \mathbf{A}^p_{dl}\,\mathbf{x}^p_{k-N_d^p} + \mathbf{B}^p_{dl}\,u^p_{k-N_d^p}, \\ y^p_k = \mathbf{C}^p_{dl}\,\mathbf{x}^p_{k-N_d^p} + \mathbf{D}^p_{dl}\,u^p_{k-N_d^p}, \end{cases} \tag{15}$$

and for the secondary path:

$$\begin{cases} \mathbf{x}^s_{k+1-N_d^s} = \mathbf{A}^s_{dl}\,\mathbf{x}^s_{k-N_d^s} + \mathbf{B}^s_{dl}\,u^s_{k-N_d^s}, \\ y^s_k = \mathbf{C}^s_{dl}\,\mathbf{x}^s_{k-N_d^s} + \mathbf{D}^s_{dl}\,u^s_{k-N_d^s}. \end{cases} \tag{16}$$

where $\mathbf{A}^p_{dl} \in \mathbb{R}^{m\times m}$, $\mathbf{B}^p_{dl} \in \mathbb{R}^{m\times 1}$, $\mathbf{C}^p_{dl} \in \mathbb{R}^{1\times m}$, $\mathbf{D}^p_{dl} \in \mathbb{R}^{1\times 1}$, $\mathbf{A}^s_{dl} \in \mathbb{R}^{n\times n}$, $\mathbf{B}^s_{dl} \in \mathbb{R}^{n\times 1}$, $\mathbf{C}^s_{dl} \in \mathbb{R}^{1\times n}$ and $\mathbf{D}^s_{dl} \in \mathbb{R}^{1\times 1}$. Here, the subscript $(\cdot)_{dl}$ indicates the corresponding delay-free system matrices.

By combining both paths, the joint state-space model is formulated as:

$$\begin{cases} \mathbf{x}'_{k+1} = \underbrace{\begin{bmatrix} \mathbf{A}^p_{dl} & 0 \\ 0 & \mathbf{A}^s_{dl} \end{bmatrix}}_{\mathbf{A}_{dl}} \mathbf{x}'_k + \begin{bmatrix} \mathbf{B}^p_{dl} \\ 0 \end{bmatrix} u^p_{k-N_d^p} + \begin{bmatrix} 0 \\ B^s_{dl} \end{bmatrix} u^s_{k-N_d^s}, \\ y_k = y^p_k - y^s_k = \underbrace{\begin{bmatrix} \mathbf{C}^p_{dl} & -\mathbf{C}^s_{dl} \end{bmatrix}}_{\mathbf{C}_{dl}} \mathbf{x}'_k + \mathbf{D}^p_{dl}\,u^p_{k-N_d^p} - \mathbf{D}^s_{dl}\,u^s_{k-N_d^s}. \end{cases} \tag{17}$$

where the augmented state vector is defined as:

$$\mathbf{x}'_k = \begin{bmatrix} \mathbf{x}^p_{k-N_d^p} \\ \mathbf{x}^s_{k-N_d^s} \end{bmatrix}. \tag{18}$$

The corresponding input sequences of primary and secondary paths are expressed as:

$$\mathbf{u}'^p = \begin{bmatrix} u^p_{k-N_d^p} \\ \vdots \\ u^p_{k+f-N_d^p} \end{bmatrix}, \qquad \mathbf{u}'^s = \begin{bmatrix} u^s_{k-N_d^s} \\ \vdots \\ u^s_{k+f-N_d^s} \end{bmatrix}. \tag{19}$$

Based on this formulation, Eq. (8) and (9) are modified as:

$$\mathbf{c}' = \mathbf{O}_{dl}\,\mathbf{x}'_k + \mathbf{M}^p_{dl}\,\mathbf{u}'^p, \qquad \mathbf{y} = \mathbf{c}' - \mathbf{M}^s_{dl}\,\mathbf{u}'^s. \tag{20}$$

where the prediction matrices $\mathbf{O}_{dl}$, $\mathbf{M}^p_{dl}$, and $\mathbf{M}^s_{dl}$ are defined as

$$\mathbf{O}_{dl} = \begin{bmatrix} \mathbf{C}_{dl}\mathbf{A}_{dl} \\ \mathbf{C}_{dl}\mathbf{A}^2_{dl} \\ \vdots \\ \mathbf{C}_{dl}\mathbf{A}^f_{dl} \end{bmatrix} \in \mathbb{R}^{f\times(m+n)}, \quad \mathbf{M}^p_{dl} = \begin{bmatrix} \mathbf{C}^p_{dl}\mathbf{B}^p_{dl} & \mathbf{D}^p_{dl} & \cdots & 0 & 0 \\ \mathbf{C}^p_{dl}\mathbf{A}^p_{dl}\mathbf{B}^p_{dl} & \mathbf{C}^p_{dl}\mathbf{B}^p_{dl} & \ddots & 0 & 0 \\ \vdots & \vdots & \ddots & \ddots & \vdots \\ \mathbf{C}^p_{dl}(\mathbf{A}^p_{dl})^{f-1}\mathbf{B}^p_{dl} & \mathbf{C}^p_{dl}(\mathbf{A}^p_{dl})^{f-2}\mathbf{B}^p_{dl} & \cdots & \mathbf{C}^p_{dl}\mathbf{B}^p_{dl} & \mathbf{D}^p_{dl} \end{bmatrix}, \tag{21}$$

and

$$\mathbf{M}^s_{dl} = \begin{bmatrix} \mathbf{C}^s_{dl}\mathbf{B}^s_{dl} & \mathbf{D}^s_{dl} & \cdots & 0 & 0 \\ \mathbf{C}^s_{dl}\mathbf{A}^s_{dl}\mathbf{B}^s_{dl} & \mathbf{C}^s_{dl}\mathbf{B}^s_{dl} & \ddots & 0 & 0 \\ \vdots & \vdots & \ddots & \ddots & \vdots \\ \mathbf{C}^s_{dl}(\mathbf{A}^s_{dl})^{f-1}\mathbf{B}^s_{dl} & \mathbf{C}^s_{dl}(\mathbf{A}^s_{dl})^{f-2}\mathbf{B}^s_{dl} & \cdots & \mathbf{C}^s_{dl}\mathbf{B}^s_{dl} & \mathbf{D}^s_{dl} \end{bmatrix}, \tag{22}$$

where $\mathbf{O}_{dl} \in \mathbb{R}^{f\times(m+n)}$ and $\mathbf{M}^p_{dl}, \mathbf{M}^s_{dl} \in \mathbb{R}^{f\times(f+1)}$.

Then, the optimal control input sequence is computed by:

$$\mathbf{u}'^{s*} = \mathbf{H}'^{-1}\mathbf{g}', \tag{23}$$

where

$$\mathbf{H}' = \mathbf{M}^{s\,T}_{dl}\mathbf{Q}\mathbf{M}^s_{dl} + \mathbf{R}, \qquad \mathbf{g}' = \mathbf{M}^{s\,T}_{dl}\mathbf{Q}\,\mathbf{c}'. \tag{24}$$

In this formulation of the state-space model, it is required that the following condition holds:

$$f < N_d \tag{25}$$

where $N_d = N_d^p - N_d^s$ denotes the delay difference between the primary and secondary paths. This condition ensures that the primary input sequence $\mathbf{u}'^p$ is available before the sequence $\mathbf{u}'^s$ is initiated. Consequently, $\mathbf{u}'^p$ can be utilized to compute the optimal controller output sequence $\mathbf{u}'^{s*}$, thereby preserving system causality.

To maximize the allowable prediction horizon f, a larger primary path delay N_d^p and a smaller secondary path delay N_d^s are desirable. On the other hand, an excessively small prediction horizon may lead to insufficient preview information and an ill-conditioned optimization problem, which may prevent reliable control solutions from being obtained in practice. Accordingly, the preferred modeling strategy is to construct the delayed system using Eqs. (15) and (2), wherein only the delay in the primary path is considered by setting $N_d^s = 0$, resulting in $N_d = N_d^p$.

2.5. Algorithm procedure

Fig. 1a illustrates the operational logic of the MPC-based ANC system. At each sampling instant k, the reference signal u_k^p is used to compute the controller output u_k^s based on a predefined state-space model and the MPC algorithm. Simultaneously, the signals u_k^p and u_k^s propagate through the physical primary path P and the secondary path S, producing the primary disturbance d_k and anti-noise a_k, respectively. The resulting measured error signal is then obtained as $e_k = d_k - a_k$.

Fig. 1b provides a detailed illustration of the sampling instants for the signals y, u^p, and u^s. In this figure, the bold curves represent the sequences $\mathbf{y}$, $\mathbf{u}^p$, and $\mathbf{u}^s$ as defined in Eq. (5) at the current instant k. The reference trajectory for the error signal y is set to zero, and the controller output u^s is subject to the saturation limits described in Eq. (13). The complete computational procedure is presented in Algorithm 1, which consists of two stages: (i) state-space model preparation, typically conducted offline, and (ii) the MPC optimization loop, executed online in real time.

For the delayed MPC strategy shown in Fig. 2a, the secondary path delay is set to $N_d^s = 0$, while the reference signal u^p is delayed by N_d instants. The bold curves in Fig. 2b denote the sequences $\mathbf{y}$, $\mathbf{u}'^p$, and $\mathbf{u}^s$ at instant k. In this configuration, if the causality condition specified in Eq. (25) is satisfied, the sequence $\mathbf{u}'^p$ remains within past instants, ensuring the feasibility of real-time computation. The corresponding computational steps for the delayed MPC approach are detailed in Algorithm 2.

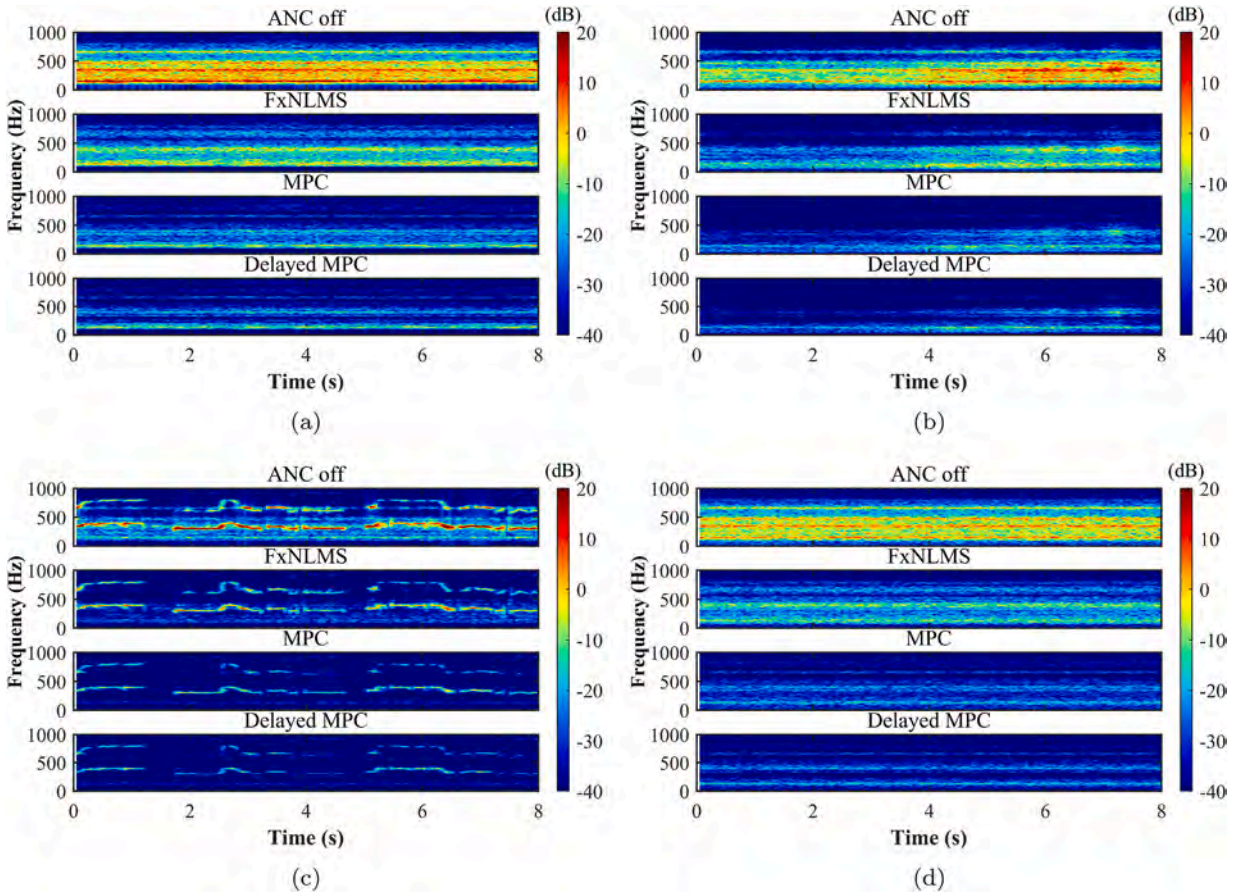

Fig. 6. Short-Time Fourier Transform of error signals for different noise types: (a) Traffic. (b) Airplane. (c) Human. (d) White. (For interpretation of the references to colour in this figure legend, the reader is referred to the web version of this article.)

Algorithm 1 MPC-based ANC algorithm.

```
/* State-Space Model Preparation */
Define the state-space matrices: A^p, B^p, C^p, D^p, A^s, B^s, C^s, D^s
Specify the weighting matrices Q, R, and the prediction horizon f
Compute the matrices O, M^p, and M^s using Eqs. (6) and (7)
/* MPC Optimization Loop */
Initialize the system state: x_1 = 0_{m+n}
for k = 1, 2, ... do
    Obtain the future disturbance sequence u^p using Eq. (5)
    Compute the optimal control sequence u^{s*} by solving Eq. (11)
    Restrict the controller output u_k^s according to the saturation constraint in Eq. (13)
    Apply the control input u_k^{s,sat}
    Update the joint system state x_{k+1} using Eq. (3)
end for
```

2.6. System identification

To define the state-space matrices, we first measured the primary and secondary paths of a Kundt's tube, as illustrated in Fig. 3. Specifically, a white noise signal was applied to the loudspeaker as the input signal x_{in}, and the corresponding output response x_{out} was recorded by the error microphone. The frequency response function was then estimated using the following expression:

$$H_{\text{meas}} = \frac{E\{X_{\text{in}}^* X_{\text{out}}\}}{E\{X_{\text{in}}^* X_{\text{in}}\}} \tag{26}$$

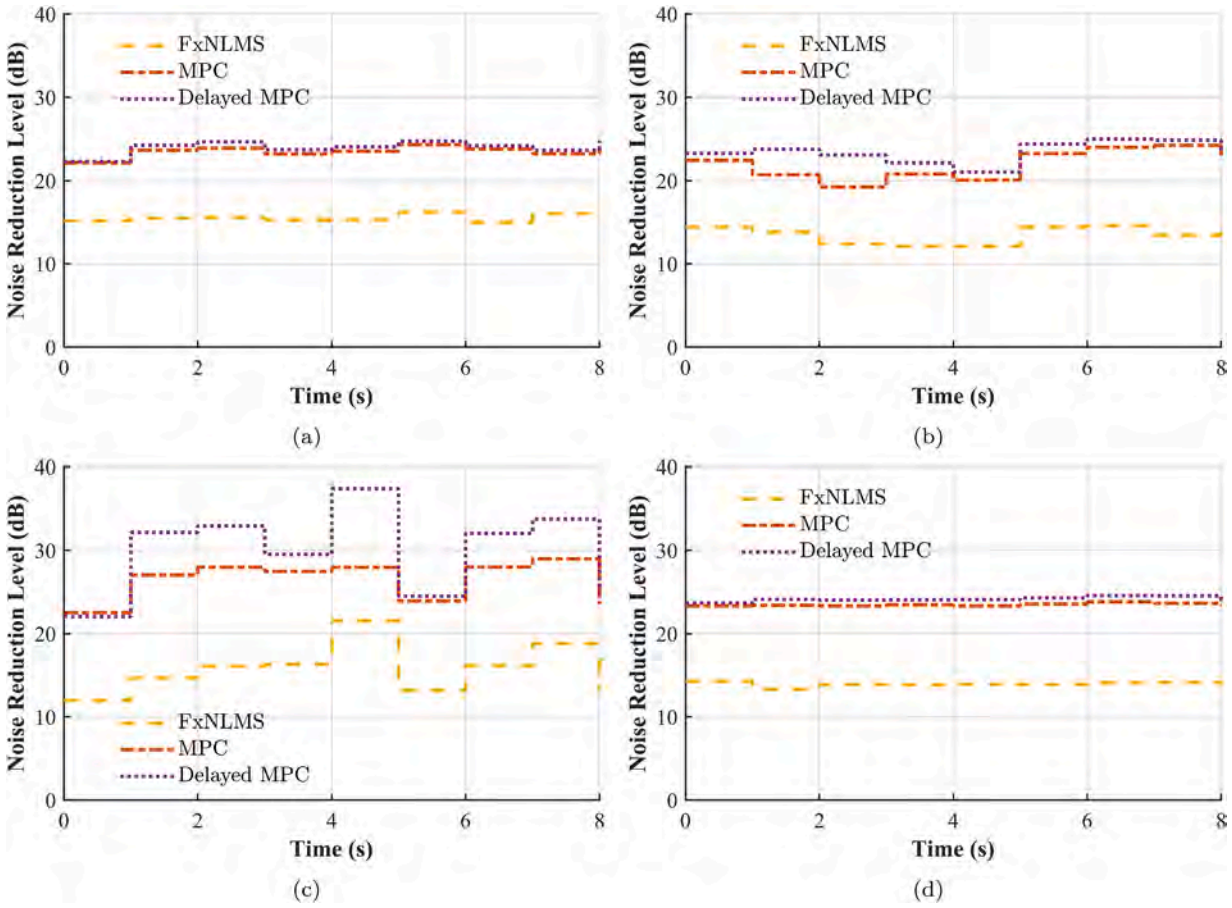

Fig. 7. Noise reduction level of error signals for different noise types: (a) Traffic. (b) Airplane. (c) Human. (d)White. (For interpretation of the references to colour in this figure legend, the reader is referred to the web version of this article.)

Algorithm 2 Delayed MPC-based ANC algorithm.

```
/* State-Space Model Preparation */
Define the state-space matrices: A^p_dl, B^p_dl, C^p_dl, D^p_dl, A^s, B^s, C^s, D^s
Specify the weighting matrices Q, R
Set the prediction horizon f such that f < N_d and N^s_d = 0
Compute the prediction matrices O_dl, M^p_dl, and M^s_dl following Eqs. (6) and (7)
/* MPC Optimization Loop */
Initialize the system state: x_{N_d+1} = 0_{m+n}
for k = N_d + 1, N_d + 2, ... do
    Acquire the past disturbance sequence u'^p using Eq. (19)
    Compute the optimal control sequence u'^{s*} by solving Eq. (23)
    Restrict the first controller output u^s_k according to the saturation constraints
    Apply the control input u^{s,sat}_k
    Update the joint system state x'_{k+1} using Eq. (17)
end for
```

where X_{in} and X_{out} denote the Fourier transforms of x_{in} and x_{out}, respectively, $(\cdot)^*$ represents the complex conjugate operation, and $E\{\cdot\}$ denotes the mathematical expectation. Only the frequency components within the range of 100–800 Hz were retained for subsequent analysis.

Subsequently, to obtain the required state-space representations for the controller design, a standard system identification procedure is performed. In this study, we utilize the vector fitting method [18] as a representative tool to estimate the plant dynamics.

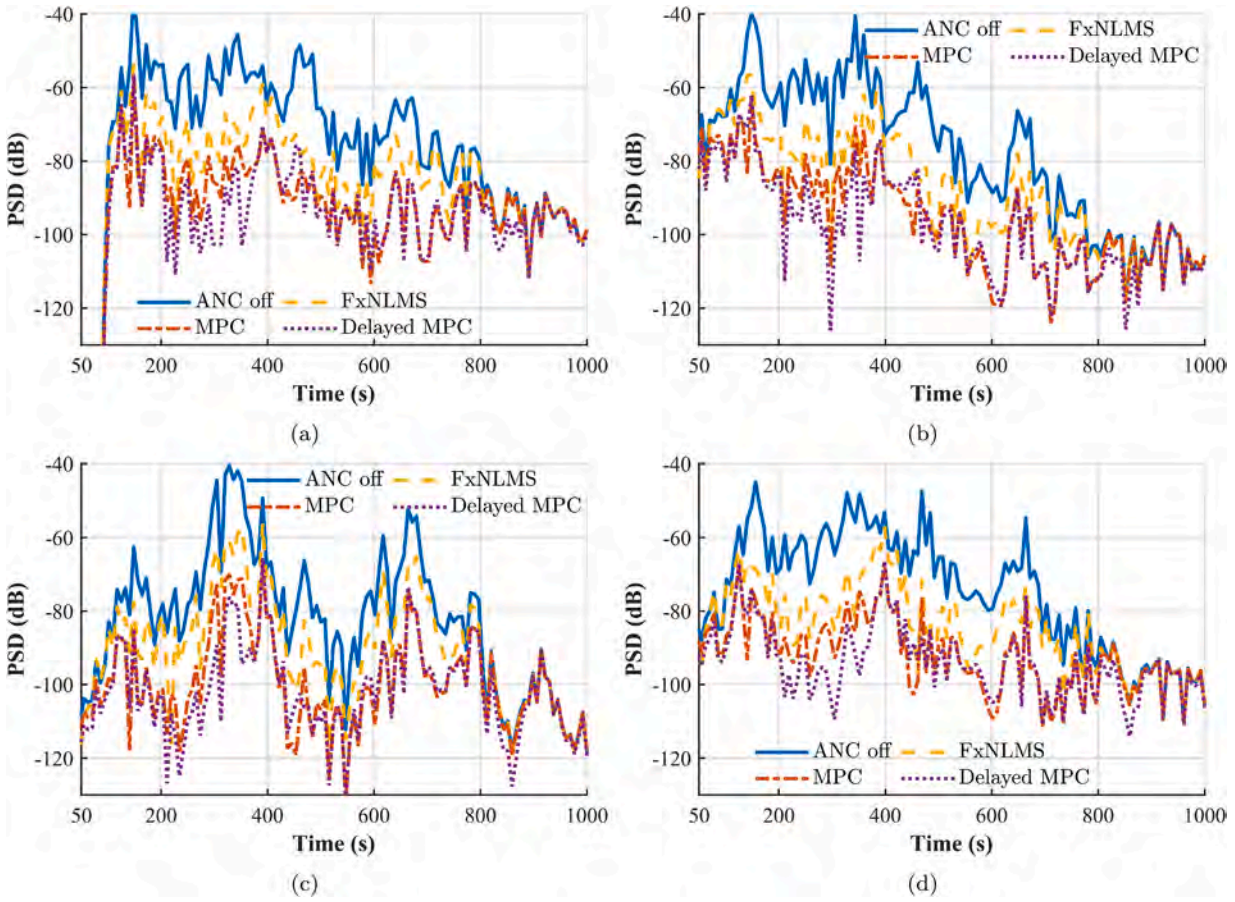

Fig. 8. Power spectral density of error signals for different noise types: (a) Traffic. (b) Airplane. (c) Human. (d) White. (For interpretation of the references to colour in this figure legend, the reader is referred to the web version of this article.)

From a formulation perspective, the proposed delayed-MPC framework is theoretically generalizable to various system identification methods, provided that the plant dynamics are captured in a state-space realization.

A discrete-time system $G(z)$ was identified from the measured frequency response H_{meas}. To determine an appropriate model order, several candidate orders were evaluated by progressively increasing the model complexity and examining the corresponding frequency-domain fitting accuracy within the 100–800 Hz frequency band. It was observed that model orders below 15 were unable to accurately reproduce the resonance peaks and phase characteristics of the measured responses, while higher-order models yielded only marginal improvements. A 15th-order model was therefore selected as a compromise between modeling accuracy and computational efficiency. The transfer function $G(z)$ takes the form

$$G(z) = \frac{b_0 + b_1 z^{-1} + \cdots + b_q z^{-q}}{1 + a_1 z^{-1} + \cdots + a_r z^{-r}}, \tag{27}$$

where $q = r = 15$. By applying the standard relation $G(z) = C(zI - A)^{-1}B + D$, the identified transfer function was converted into an equivalent state-space representation, as shown in Eqs. (1) and (2). The fitted curves presented in Fig. 3 demonstrate the satisfactory accuracy of the estimated state-space models.

For the delayed MPC configuration, we set $N_d^s = 0$ and $N_d^p = 10$, corresponding to a delay of $T_d = N_d/f_s = 2.5$ ms. For the primary path, the delayless frequency response $H^p_{\text{delayless}}$ and its corresponding state-space model are illustrated in Fig. 4a. The system delay is then incorporated by multiplying the delayless response with z^{-N_d}, resulting in $H^p_{\text{delayless}} \cdot z^{-N_d}$.

Fig. 4b compares the unit impulse responses of the estimated state-space models corresponding to H^p_{meas} and $H^p_{\text{delayless}} \cdot z^{-N_d}$. As expected, the impulse response of the delayed model starts after $t = 2.5$ ms. Beyond this point, the two responses exhibit an almost perfect overlap, indicating the accuracy and consistency of the delayed model with respect to the original measurement.

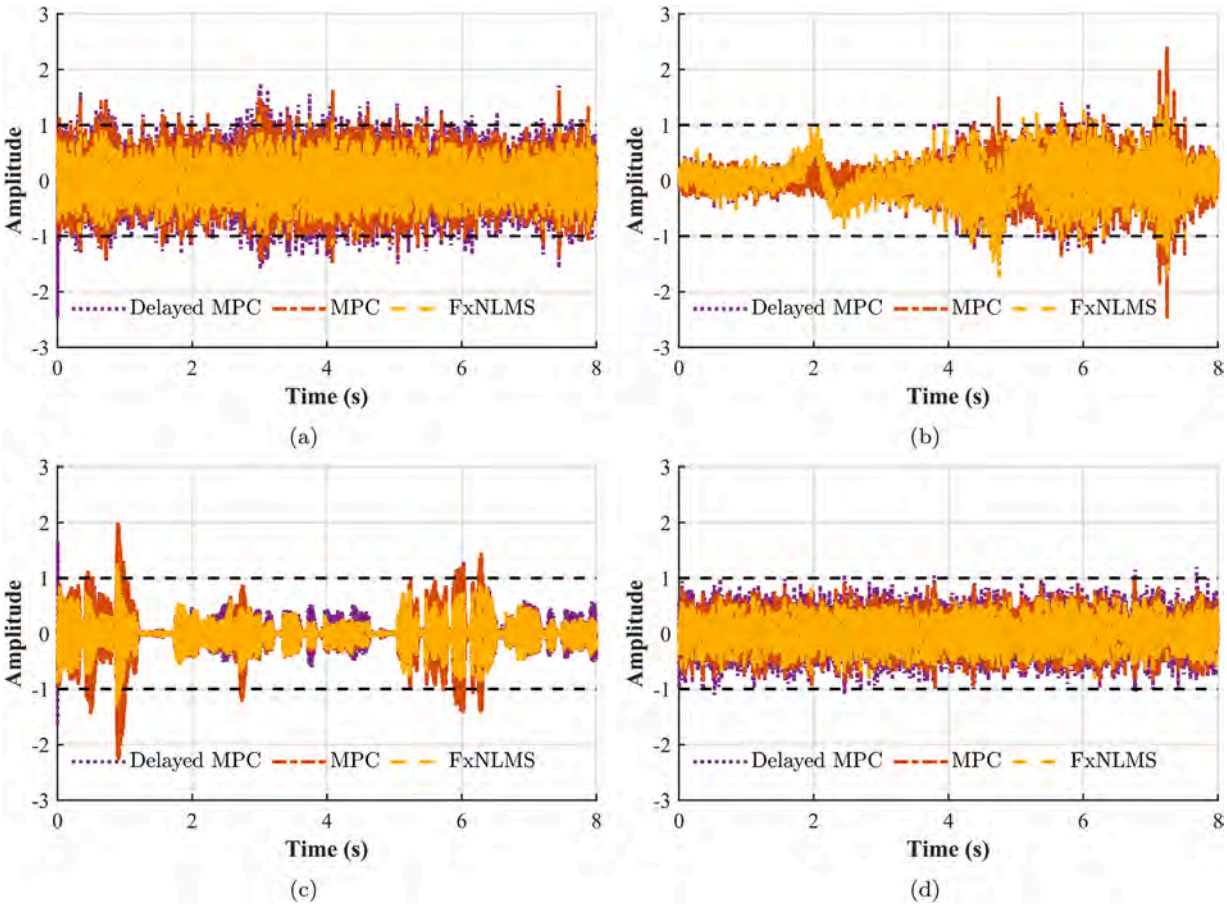

Fig. 9. Controller output u^s before saturation for different noise types: (a) Traffic. (b) Airplane. (c) Human. (d) White.

3. Numerical simulation

3.1. Parameters setup

The sampling rate is set to $f_s = 4\,\text{kHz}$. The reference signals consist of four realistic audio clips selected from [19] and the Acoustic Event Dataset [20], in addition to white noise, each with a duration of 8 s. The default amplitude of the reference signals is set to $A_{\max} = 0.2$. To investigate the impact of control saturation described in Eq. (13), a higher amplitude value of $A_{\max} = 0.8$ is also examined in Section 3.3.

The controller weighting matrices are defined as $\mathbf{Q} = \alpha\mathbf{I}$ and $\mathbf{R} = \beta\mathbf{I}$, with $\alpha = 1$ and $\beta = 0.001$. Here, $\mathbf{Q}$ penalizes the predicted residual error to promote noise attenuation, while $\mathbf{R}$ penalizes the control effort to limit excessive control amplitudes and mitigate actuator saturation. Both the prediction and control horizons are set to $f = 9$. The state-space model orders of the primary and secondary paths are $m = 15$ and $n = 15$, respectively. The saturation limits for the control input are specified as $u^s_{\max} = 1$ and $u^s_{\min} = -1$.

For the FxNLMS algorithm, the adaptive filter length is set to $K = 64$, allowing for relatively fast convergence. To approximate the steady-state optimal solution of FxNLMS, the adaptive filter was first trained by canceling white noise until convergence. The resulting filter coefficients were then used to initialize the FxNLMS algorithm for all subsequent simulations and experiments. The filter length L of the estimated secondary path is 512. The default step size is chosen as $\mu = 0.001$ to ensure stable convergence in both simulation and experimental scenarios.

3.2. Noise reduction performance

Fig. 5 presents the error signals obtained by different ANC algorithms. The labels 'MPC' and 'Delayed MPC' refer to Algorithms 1 and 2, respectively. As shown in Fig. 5a, both MPC and Delayed MPC achieve substantial noise reduction. Owing to the optimal initialization of the control filter, FxNLMS exhibits stable tracking performance across various reference signals, particularly for traffic and white noise. Nevertheless, its noise reduction capability remains inferior to that of the proposed MPC schemes under these conditions. Regarding the airplane noise in Fig. 5b, when the signal amplitude fluctuates after $t = 4$ s, the error signals associated with

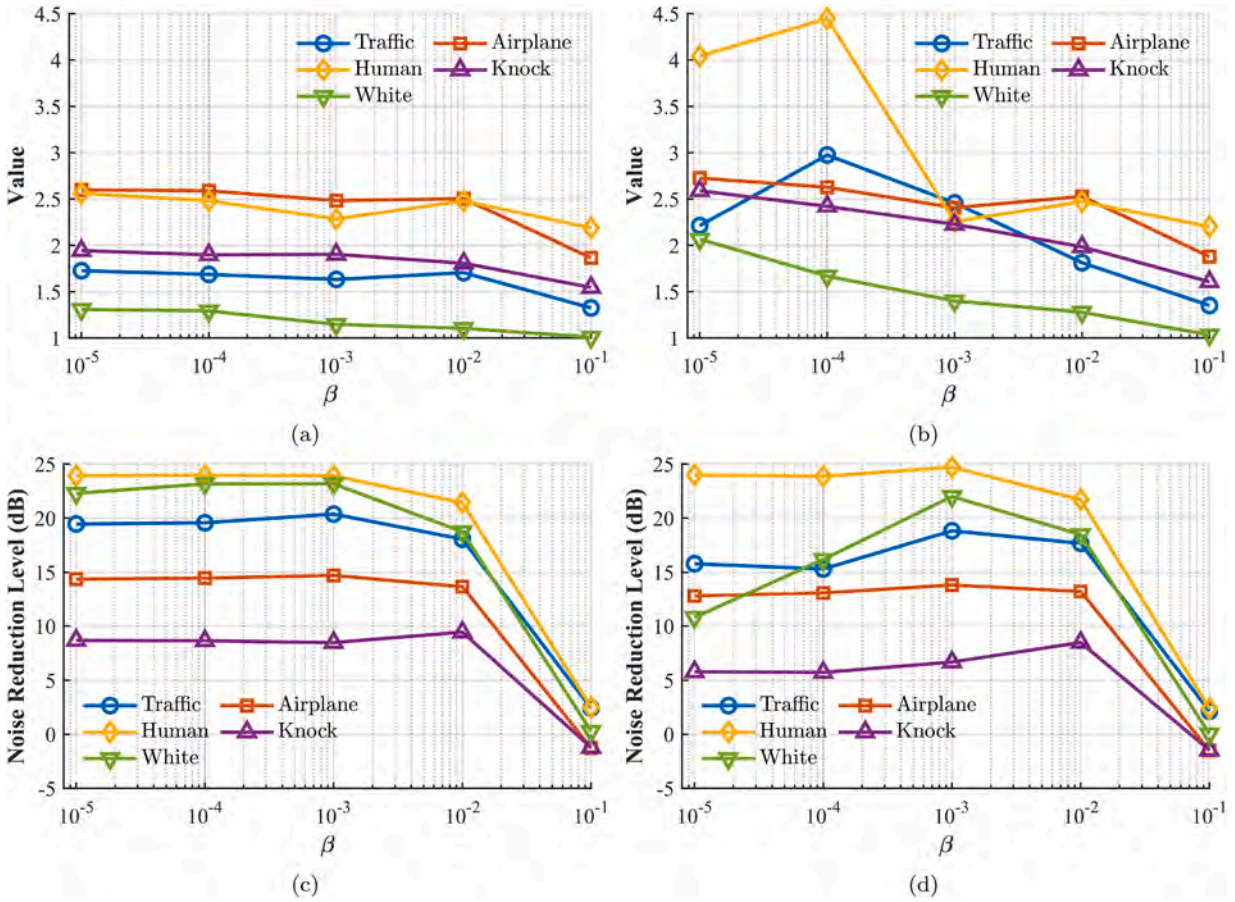

Fig. 10. Effect of weighting matrix **R** on control saturation and noise reduction performance. (a), (b) Maximum amplitudes of optimized controller outputs; (c), (d) Noise reduction levels. (a), (c) MPC; (b), (d) Delayed MPC. (For interpretation of the references to colour in this figure legend, the reader is referred to the web version of this article.)

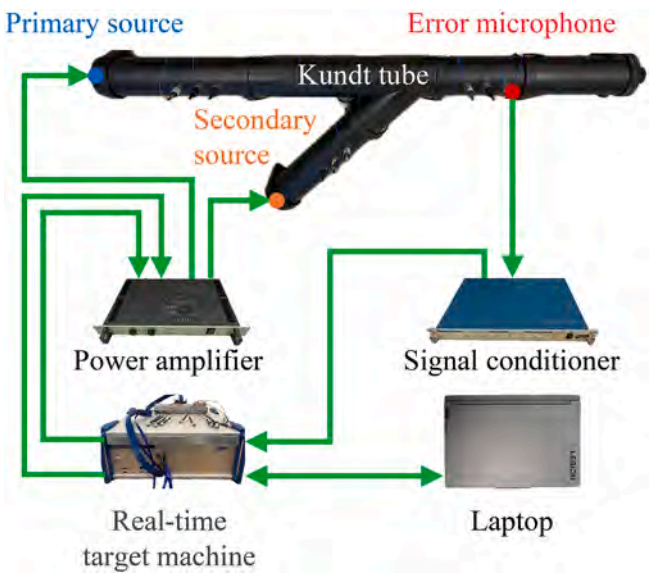

Fig. 11. Experimental setup.

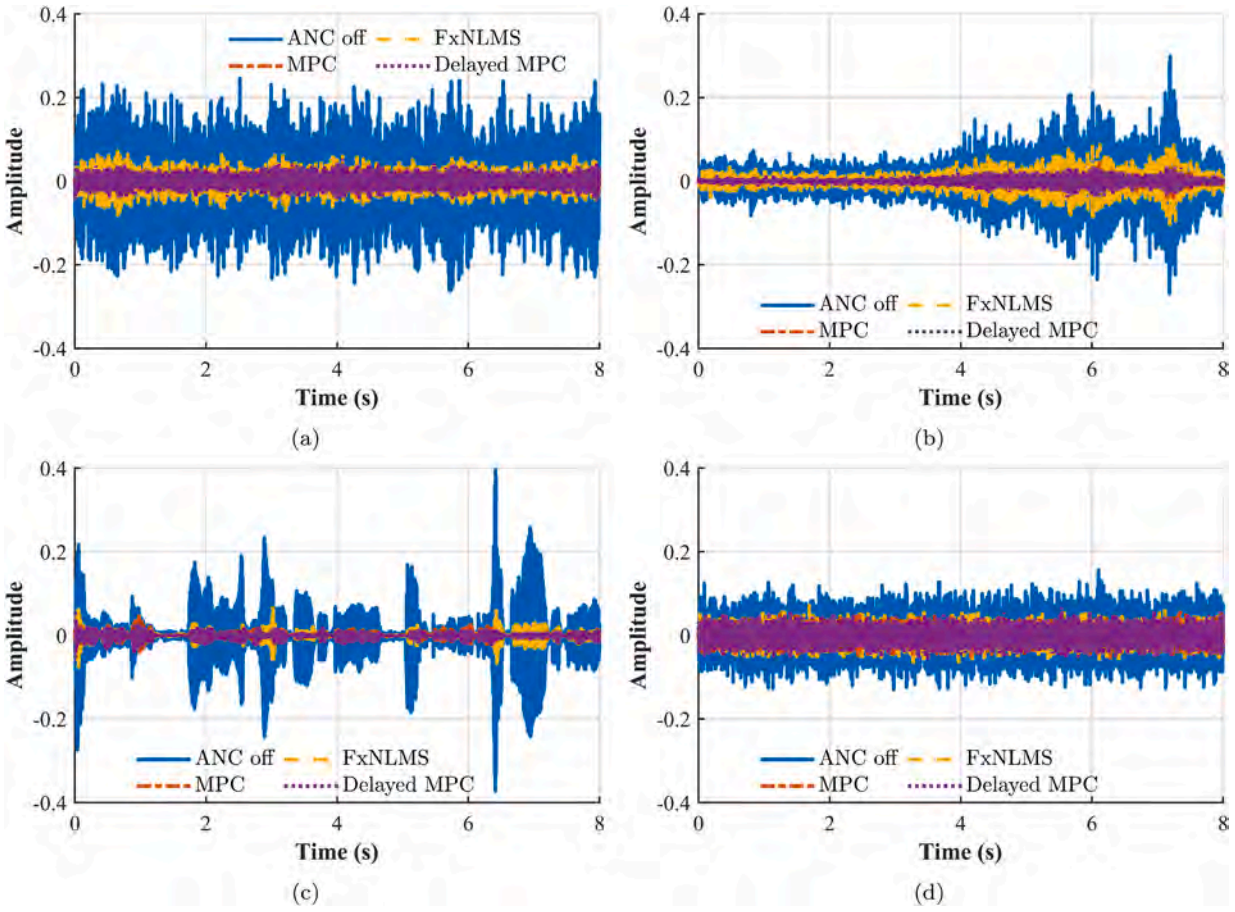

Fig. 12. Error signals for different noise types: (a) Traffic. (b) Airplane. (c) Human. (d) White. (For interpretation of the references to colour in this figure legend, the reader is referred to the web version of this article.)

MPC and Delayed MPC display minor fluctuations, whereas those from FxNLMS fluctuate significantly. In cases of human noise, which exhibits more abrupt variations, MPC and Delayed MPC continue to demonstrate superior robustness and effective noise suppression.

Fig. 6 displays the short-time Fourier transform (STFT) spectrograms of the error signals. When ANC is disabled, traffic, airplane and white noise exhibit continuous spectral content, whereas human noise displays abrupt changes at various time instances. The dominant frequency components are concentrated roughly between 100 Hz and 800 Hz. Both MPC and Delayed MPC consistently achieve superior noise attenuation across the entire frequency range compared to FxNLMS.

Fig. 7 presents the noise reduction level (NRL), defined as $\mathrm{NRL} = 10\log_{10}\left(\frac{\sum d^2}{\sum e^2}\right)$, calculated every second. For traffic, airplane, and white noises, the proposed MPC and Delayed MPC schemes maintain steady NRL values ranging from approximately 20 dB to 25 dB throughout the entire simulation, whereas that of FxNLMS remains within the range of 11–17 dB. In the case of human noise, the NRL exhibits more pronounced fluctuations, which can be attributed to the intense and irregular variations in its frequency content.

Fig. 8 presents the power spectral density (PSD) of the error signals. Across all tested noise types, both MPC and Delayed MPC achieve broadband noise reduction of approximately 20 dB across most of the frequency range.

Table 2 summarizes the overall NRL values obtained from Figs. 5 to 8, including additional results for impulsive knock reference noise. With its control filter operating in the steady state, FxNLMS yields noise reductions ranging from 13.4 dB to 15.6 dB. For comparison, we also evaluated an offline-designed FIR controller constructed from the sampled frequency-response ratio between the identified primary and secondary paths, approximating the inverse relationship between the two paths. Specifically, the frequency-response ratio $P(\omega)/S(\omega)$ was transformed to the time domain using an inverse Fourier transform and truncated to obtain a finite-length FIR controller [21]. The frequency responses of the physical primary and secondary acoustic paths P and S are denoted by $P(\omega)$ and $S(\omega)$, respectively, where ω represents the discrete angular frequency. The resulting FIR controller is fixed and provides noise reduction levels of approximately 4-5 dB, which are significantly lower than those achieved by FxNLMS and the proposed MPC approaches. In comparison, MPC achieves NRLs between 21.9 dB and 26.8 dB for different noises, while the Delayed MPC achieves reductions ranging from 23.1 dB to 29.0 dB.

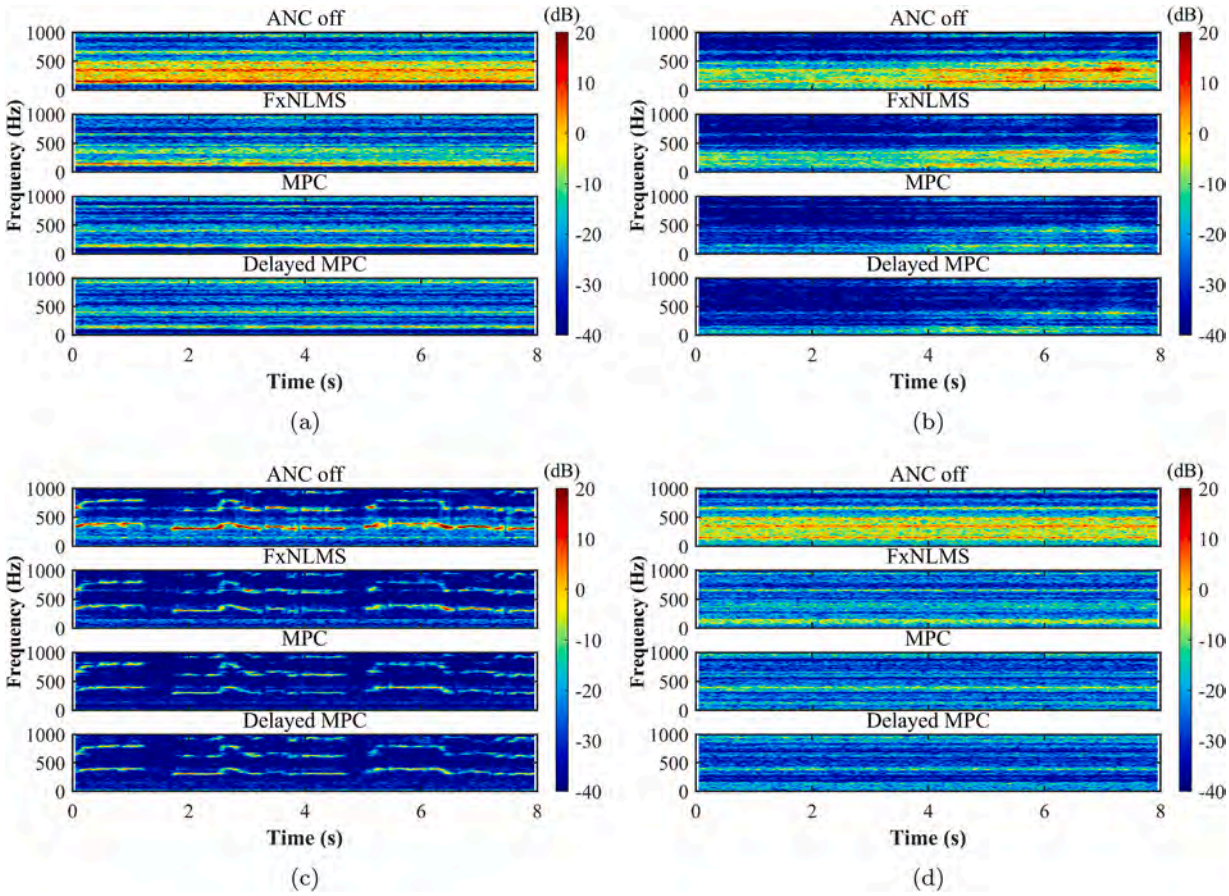

Fig. 13. Short-time fourier transform of error signals for different noise types: (a) Traffic. (b) Airplane. (c) Human. (d) White. (For interpretation of the references to colour in this figure legend, the reader is referred to the web version of this article.)

Table 2
Noise reduction levels (dB) obtained from simulations using different control strategies. $A_{max} = 0.2$..

Control strategies	Noise type				
	Traffic	Airplane	Human	Knock	White
Offline FIR ($P(\omega)/S(\omega)$)	4.87	4.13	4.79	4.61	4.34
FxNLMS	15.50	13.63	15.57	13.42	13.91
MPC	23.40	22.63	26.81	21.85	23.57
Delayed MPC	23.84	23.79	29.03	23.14	24.15

3.3. Influence of saturation

While the control inputs of FxNLMS and MPC did not trigger saturation at $A_{max} = 0.2$, the results for $A_{max} = 0.8$ are presented in Table 3. The offline FIR controller is also included for comparison, and its noise reduction levels remain approximately the same as those reported for $A_{max} = 0.2$. For FxNLMS, the NRLs at $A_{max} = 0.8$ are identical or highly similar to those at $A_{max} = 0.2$, with the exception of airplane and impulsive knock noises. In contrast, the MPC scheme at $A_{max} = 0.8$ exhibits NRL values comparable to those obtained at $A_{max} = 0.2$ only for white noise, because the controller output seldom triggers saturation under this specific noise condition.

Fig. 9 shows the controller outputs prior to the application of saturation limits. Values exceeding the predefined bounds (indicated by two horizontal dashed lines) are subsequently clipped. The controller outputs for white noises remain mostly within the linear region and are only marginally affected by saturation. In contrast, the control signals for airplane noise frequently clip against the saturation bounds, resulting in a substantial degradation in noise attenuation performance. Specifically, the noise reduction levels drop by approximately 8 dB and 10 dB for the MPC and Delayed MPC schemes, respectively, as shown in Table 3, compared to the corresponding values in Table 2.

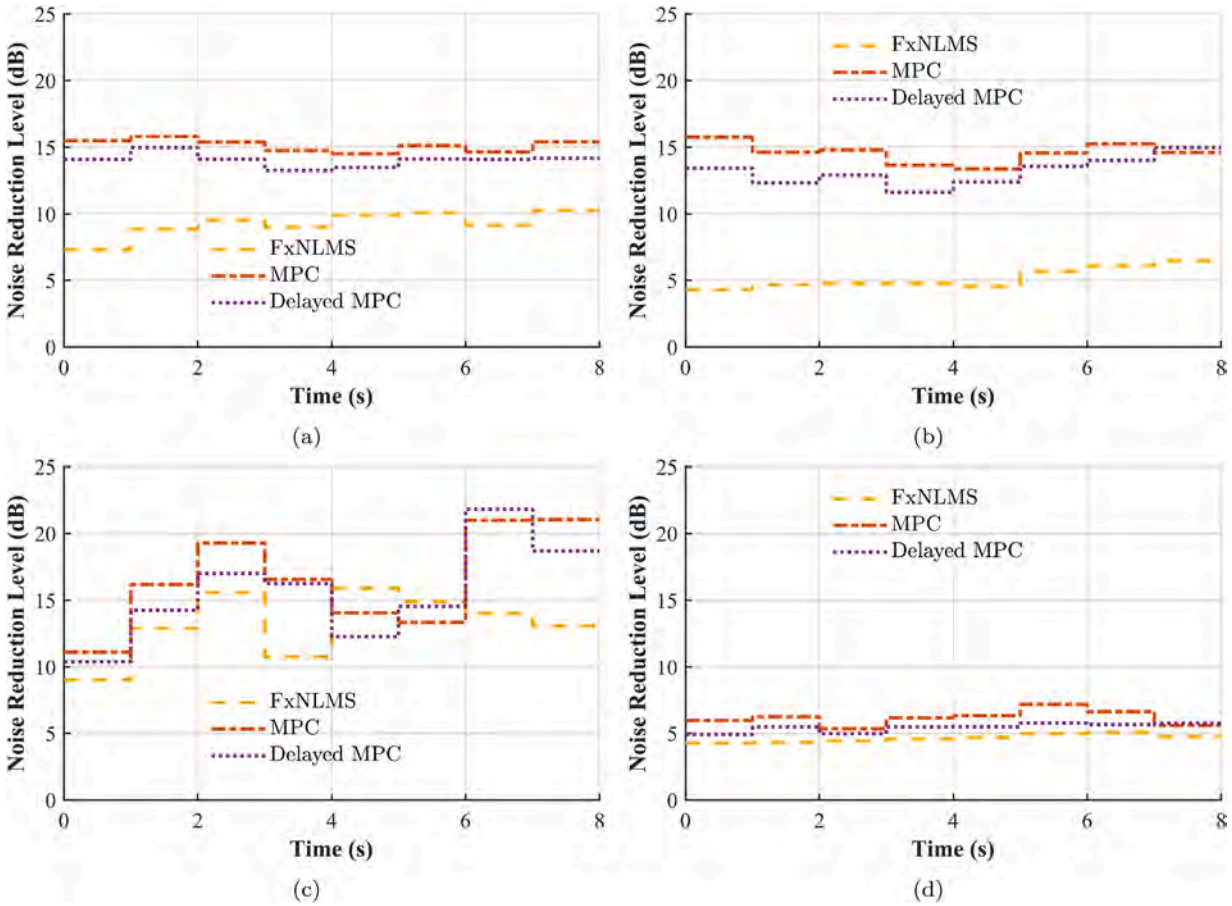

Fig. 14. Noise reduction level of error signals for different noise types: (a) Traffic. (b) Airplane. (c) Human. (d) White. (For interpretation of the references to colour in this figure legend, the reader is referred to the web version of this article.)

Table 3
Noise reduction levels (dB) obtained from simulations using different control strategies. $A_{\max} = 0.8$..

Control strategies	Noise type				
	Traffic	Airplane	Human	Knock	White
Offline FIR ($P(\omega)/S(\omega)$)	4.87	4.13	4.79	4.61	4.25
FxNLMS	15.49	9.98	15.47	5.79	13.94
MPC	20.37	14.71	23.90	8.48	23.17
Delayed MPC	18.83	13.83	24.70	6.68	22.00

To further elucidate the influence of the weighting matrix $\mathbf{R}$ on the MPC behavior, α is held constant while β is varied to investigate their impact on control amplitude, saturation, and noise attenuation performance. The weighting matrices can also be tuned to regulate the magnitude of the optimized control inputs. The resulting peak values of the control input u^s are illustrated in Fig. 10a and b. As β increases, the control amplitudes decrease due to the stronger penalty imposed by $\mathbf{R}$ on $\mathbf{u}^{s*}$ and $\mathbf{u}'^{s*}$. Notably, for $\beta < 0.001$, the peak amplitudes under Delayed MPC exhibit larger variations than those under standard MPC.

Although a larger β reduces control amplitudes and mitigates saturation, it does not necessarily improve noise attenuation. A higher β weights the control effort more heavily in the cost function, leading to more conservative control actions and potentially less effective suppression of $\mathbf{y}$, thereby degrading attenuation performance. Figs. 10c and d summarize the combined effects of weighting and saturation on noise reduction. For $\beta \geq 0.001$, both MPC variants achieve comparable noise reduction levels. However, when $\beta < 0.001$, Delayed MPC yields lower noise reduction than standard MPC, which is consistent with the higher peak amplitudes observed in Fig. 10b that lead to more severe saturation.

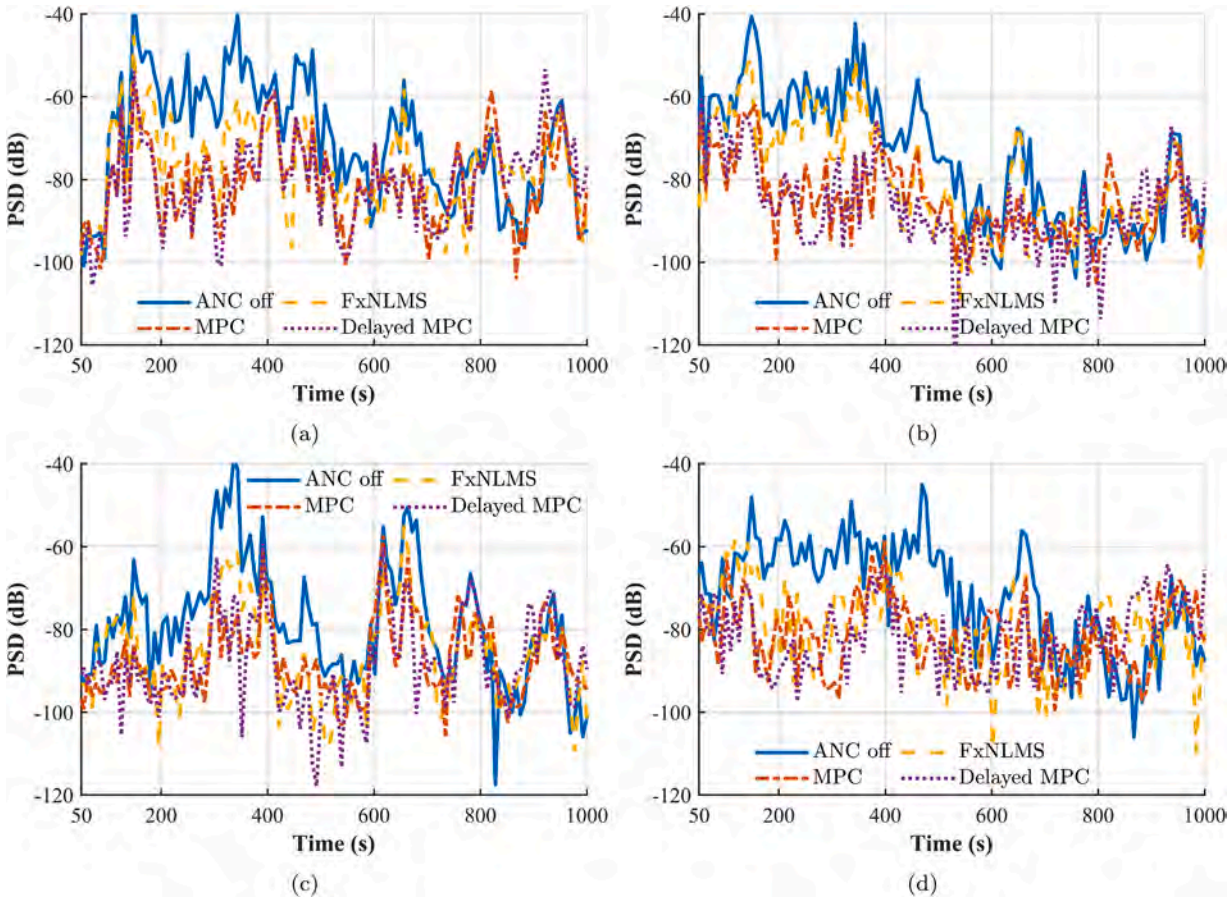

Fig. 15. Power spectral density of error signals for different noise types: (a) Traffic. (b) Airplane. (c) Human. (d) White. (For interpretation of the references to colour in this figure legend, the reader is referred to the web version of this article.)

4. Experimental validation

4.1. Experimental setup

Fig. 11 depicts the experimental configuration used to validate the real-time performance of the proposed MPC-based ANC approach. A Kundt's tube was used as the test rig, where its primary and secondary acoustic paths correspond to P and S illustrated in Figs. 1a and 2a, respectively. The control algorithms were implemented in MATLAB/Simulink and executed on a Speedgoat real-time target machine. All parameters, including sampling rate, horizon, weighting matrices, and saturation limits, were identical to those specified in the numerical simulations of Section 3.

4.2. Noise reduction performance

Fig. 12 compares the error signals obtained from real-time experiments. Due to background noise, modeling inaccuracies, and measurement errors, the experimental error signals exhibit slight deviations from the simulated results presented in Fig. 5. Both MPC variants achieve superior noise reduction compared to FxNLMS and exhibit near-instantaneous convergence, as the optimal control input is computed analytically without the need for the iterative adaptation inherent in FxNLMS.

Fig. 13 presents the corresponding STFT spectrograms. As the estimated path models are only valid over 100–800 Hz, error components outside this band remain largely unattenuated, which accounts for the discrepancies observed between the experimental and numerical results.

As illustrated in Fig. 14, all algorithms exhibit consistent and stable control performance, although the experimental NRL values are lower than the numerical simulations shown previously.

Fig. 15 shows the PSDs of the error signals. With ANC disabled, the experimental PSDs from 100 Hz to 800 Hz align closely with the numerical results in Fig. 8, confirming that the simulations provide a reliable reference for the experiments. However, the experimental PSDs exhibit additional peaks between 800 Hz and 1000 Hz that were not included in the simulations. When ANC is active under MPC and Delayed MPC, the overall PSD trends remain consistent with Fig. 8, but the discrepancy between experiment

Table 4
Noise reduction levels (dB) obtained from experiments using different algorithms.

Algorithm	$A_{\max}$	Noise type				
		Traffic	Airplane	Human	Knock	White
FxNLMS	0.2	11.24	7.66	15.36	–	6.62
	0.8	11.33	–	12.67	–	7.27
MPC	0.2	16.90	16.31	18.61	15.50	7.94
	0.8	16.03	11.74	16.99	6.06	12.93
Delayed MPC	0.2	15.77	15.39	17.82	13.69	7.22
	0.8	12.52	11.39	16.17	4.44	11.09

Table 5
Computational complexity of FxNLMS and (Delayed) MPC algorithms.

Algorithm	FxNLMS	(Delayed) MPC
$\times/\div$	$3K+L+2$	$f(2f+m+n+1)+m(m+1)+n(n+1)$
$+/-$	$2K+L-1$	$f(2f+m+n-2)+m(m-1)+n(n-1)+2$
Complexity	$O(3K+L)$	$O(2f^2+f(m+n)+m^2+n^2)$

and simulation increases at higher frequencies. Since higher frequencies are more sensitive to phase mismatches, it may stem from phase errors between the true acoustic paths and their estimated models.

Table 4 summarizes the experimental NRL values for all reference signals. FxNLMS is unable to suppress impulsive knock noise effectively. In contrast, the Delayed MPC outperforms FxNLMS by approximately 2.5–7.7 dB in cases of traffic, airplane, and human noises, while maintaining robust attenuation for knock noise. Increasing the reference amplitude to $A_{\max} = 0.8$ introduces saturation that degrades the reduction performance for non-white signals, whereas white noise remains largely unaffected owing to its uniform spectral content and lower peak amplitude; at the same time, the larger signal amplitude reduces the relative impact of background noise, slightly enhancing noise reduction.

4.3. Computational complexity

Table 5 summarizes the per-sample computational load of FxNLMS and (Delayed) MPC. In FxNLMS, the dominant cost arises from filtering through the estimated secondary path of length L and the adaptive filter of length K. In contrast, the complexity of (Delayed) MPC is determined by the state-space dimensions m and n and the prediction horizon f. Consequently, FxNLMS has complexity $O(3K+L)$, while (delayed) MPC has $O(2f^2+f(m+n)+m^2+n^2)$. For the parameter values used in this work (see Section 3.1), FxNLMS requires approximately 706 multiplications per sample compared to about 921 for (delayed) MPC, representing only a modest increase in computational effort.

5. Conclusion

In this paper, we have developed an ANC scheme based on a complete state-space representation and a standard MPC algorithm. By incorporating the primary-path delay into the model, we eliminate the need for an external disturbance predictor and thus remove any restriction on the nature of the reference noise. Moreover, the analytical solution of the unconstrained MPC problem can be computed in closed form, avoiding the use of online quadratic programming and yielding a computational complexity on par with FxNLMS. Numerical simulations and real-time experiments demonstrate that the proposed method significantly outperforms FxNLMS in noise reduction and robustness across various reference signals, with essentially no convergence delay.

Future work will focus on developing adaptive MPC variants that update the primary and secondary path models online, further improving performance under changing acoustic conditions.

CRediT authorship contribution statement

Chao Liang: Writing – review & editing, Writing – original draft, Validation, Software, Resources, Methodology, Investigation, Formal analysis, Data curation, Conceptualization; **Francesco Ripamonti:** Writing – review & editing, Writing – original draft, Validation, Supervision, Resources, Formal analysis, Data curation, Conceptualization; **Hamid Reza Karimi:** Writing – review & editing, Writing – original draft, Validation, Project administration, Funding acquisition, Conceptualization; **Marek Pawełczyk:** Writing – review & editing, Validation, Supervision, Formal analysis, Conceptualization.

Data availability

Data will be made available on request.

Declaration of competing interest

The authors declare that they have no known competing financial interests or personal relationships that could have appeared to influence the work reported in this paper.

Acknowledgement

The work was supported by the project IN-NOVA: Active reduction of noise transmitted into and from enclosures through encapsulated structures, which has received funding from the European Union's Horizon Europe program under the Marie Sklodowska-Curie grant agreement no. 101073037 and in part by the Italian Ministry of University and Research under grant "Learning-based Model Predictive Control by Exploration and Exploitation in Uncertain Environments" (PRIN PNRR 2022 fund, ID P2022EXP2W).

References

[1] L. Lu, K.-L. Yin, R.C. de Lamare, Z. Zheng, Y. Yu, X. Yang, B. Chen, A survey on active noise control in the past decade-Part I: linear systems, Signal Process. 183 (2021). https://doi.org/10.1016/j.sigpro.2021.108039
[2] Y. Guo, D. Shi, X. Shen, J. Ji, W.-S. Gan, A survey on adaptive active noise control algorithms overcoming the output saturation effect, Signal Process. 222 (2024). https://doi.org/10.1016/j.sigpro.2024.109525
[3] Y. Liu, Z. Lei, Review of advances in active impulsive noise control with focus on adaptive algorithms, Appl. Sci. Basel 14 (3) (2024). https://doi.org/10.3390/app14031218
[4] G. Takács, B. Rohal'-Ilkiv, Model predictive vibration control: efficient constrained MPC vibration control for lightly damped mechanical structures, Springer Science & Business Media, 2012.
[5] K. Henrioulle, W. Dehandschutter, P. Sas, Design of an active noise control system using a distributed actuator, Flow Turbul. Combust. 61 (1998) 189–209.
[6] R.V. Lopes, M. Nunes, A. Murilo, Active noise control in duct using a constrained state-space modelo predictive control, in: 23rd ABCM International Congress of Mechanical Engineering–COBEM, Rio De Janeiro, 2015.
[7] L. Wang, J.A. Rossiter, Disturbance rejection and set-point tracking of sinusoidal signals using generalized predictive control, in: 2008 47th IEEE Conference on Decision and Control, IEEE, 2008, pp. 4079–4084.
[8] X. Li, W. Chen, Z. Liu, C. Lu, M. Sun, A survey on filtered-x least mean square-based active noise control systems with emphasis on reducing computational complexity, EURASIP J. Adv. Signal Process. 2023 (1) (2023) 128.
[9] W. Chen, Z. Liu, L. Hu, X. Li, Y. Sun, C. Cheng, S. He, C. Lu, A low-complexity multi-channel active noise control system using local secondary path estimation and clustered control strategy for vehicle interior engine noise, Mech. Syst. Signal Process. 204 (2023) 110786.
[10] A.G. Wills, D. Bates, A.J. Fleming, B. Ninness, S.O.R. Moheimani, Model predictive control applied to constraint handling in active noise and vibration control, IEEE Trans. Contr. Syst. Technol. 16 (1) (2007) 3–12.
[11] S.-M. Moon, D.G. Cole, R.L. Clark, Real-time implementation of adaptive feedback and feedforward generalized predictive control algorithm, J. Sound Vib. 294 (1–2) (2006) 82–96.
[12] N. Mohseni, T.W. Nguyen, S.A.U. Islam, I.V. Kolmanovsky, D.S. Bernstein, Active noise control for harmonic and broadband disturbances using RLS-based model predictive control, in: 2020 American Control Conference (ACC), IEEE, 2020, pp. 1393–1398.
[13] M. Kamaldar, N. Mohseni, S. Islam, D.S. Bernstein, A numerical and experimental investigation of predictive cost adaptive control for noise and vibration suppression, Mech. Syst. Signal Process. 221 (2024) 111711.
[14] A. Bemporad, M. Morari, V. Dua, E.N. Pistikopoulos, The explicit linear quadratic regulator for constrained systems, Automatica 38 (1) (2002) 3–20.
[15] R.A. Bartlett, A. Wachter, L.T. Biegler, Active set vs. interior point strategies for model predictive control, in: Proceedings of the 2000 American Control Conference. ACC (IEEE Cat. No. 00CH36334), 6, IEEE, 2000, pp. 4229–4233.
[16] M.S.K. Lau, S.-P. Yue, K.V. Ling, J.M. Maciejowski, A comparison of interior point and active set methods for FPGA implementation of model predictive control, in: 2009 European Control Conference (ECC), IEEE, 2009, pp. 156–161.
[17] Q.-Z. Zhang, W.-S. Gan, A model predictive algorithm for active noise control with online secondary path modelling, J. Sound Vib. 270 (4–5) (2004) 1056–1066.
[18] Z. Drmac, S. Gugercin, C. Beattie, Quadrature-based vector fitting for discretized h_2 approximation, SIAM J. Sci. Comput. 37 (2) (2015) A625–A652.
[19] Z. Luo, D. Shi, W.-S. Gan, A hybrid sfanc-fxnlms algorithm for active noise control based on deep learning, IEEE Signal Process. Lett. 29 (2022) 1102–1106.
[20] N. Takahashi, M. Gygli, B. Pfister, L. Van Gool, Deep convolutional neural networks and data augmentation for acoustic event detection, arXiv preprint arXiv:1604.07160 (2016).
[21] D. Shi, W.-S. Gan, B. Lam, S. Wen, Feedforward selective fixed-filter active noise control: algorithm and implementation, IEEE/ACM Trans. Audio Speech Lang. Process. 28 (2020) 1479–1492.